Materials Science in Semiconductor Processing 159 (2023) 107363

Contents lists available at ScienceDirect

Materials Science in Semiconductor Processing

journal homepage: www.elsevier.com/locate/mssp

A lead-free environment-friendly material for optoelectronic and photocatalytic applications: A computational approach

Seerat Fatima [a], Hafiz Muhammad Naeem Ullah [b], Abrar Ahmad Zafar [a], Zahid Usman [c], M.U. Farooq [c], Muhammad Rizwan [d,*]

[a] Department of Physics, University of the Punjab, Lahore, Pakistan
[b] Research Center of Materials Science, Beijing Key Laboratory of Construction Tailorable Advanced Functional Materials and Green Applications, Beijing Institute of Technology, Beijing, 100081, PR China
[c] Department of Physics, Division of Science and Technology, University of Education, Lahore, Pakistan
[d] School of Physical Sciences, University of the Punjab, Lahore, Pakistan

ARTICLE INFO

Keywords:
Fluoride perovskites
Photocatalysis
Optical properties
Elastic properties
Mechanical properties

ABSTRACT

The structural, optoelectronic, and photocatalytic properties of $KCaF_{3-x}Br_x$, where x indicates Br concentration (x = 0, 0.6, 1.2, 1.8, 2.4, 3.0), are described here using density functional theory. Computed structural and optoelectronic results for pristine c-$KCaF_3$ are well consistent with existing literature. Bandgap was engineered by impurity inclusion such that the proposed material changes its bandgap for both generalized gradient approximation (GGA) and Heyd, Scuseria, and Ernzerhof hybrid functional (HSE03) formalism from 5.638 eV to 3.807 eV and from 8.538eV to 2.772 eV respectively. One of the most important criteria for proposing a new end material is structural and mechanical stability, thus the tolerance factor and Born's requirements were used to establish the end materials' stable cubic nature. Optical parameters such as dielectric function, reflection and absorption coefficient, refractive index, and energy loss function are calculated and analyzed up to the photon energy range of 0–35 eV. A redshift was observed whereas the refractive index values for different concentration shows continuous change except for x = 2.6. The highest value of reflectivity is observed for $KCaBr_3$ making it useful for several thermoelectric applications. Photocatalytic properties were predicted using a band edge diagram, indicating that the presented series of materials is a useful candidate for hydrogen evolution reaction (HER), and oxygen evolution reaction (OER). Br substitution at the anionic site of c-$KCaF_3$ has been reported first ever, with promising optical, elastic, and photocatalytic properties that will inspire further research on this material.

1. Introduction

The thirst for knowledge and craze for a secure and better future always drive researchers and scientists to design and discover new end materials with enhanced and fascinating properties. Advanced perovskite, synthesized by doping, gained remarkable attention due to its wide applications [1]. From the perovskite materials family, the cubic structure has the generic form of ABX_3 where A and B are cations of different radii and X can be from anionic oxygen or halogens [1,2]. ABF_3, a generic form for fluoro-perovskites, due to its fascinating nature and a wide area of application in energy conversion, storage materials, luminescence capacitors, piezoelectric systems, especially in vacuum-ultraviolet transport lenses, and transport optical coatings gained considerable attention in last few years [3–5]. Among fluoro perovskites, ternary fluorides like KCa F_3 are frequently studied because of their amazing properties such as optoelectronic and elastic properties, ferromagnetic, and nonmagnetic insulator behaviors, and chemical properties [6]. KCa F_3 also possessed a strong ionic behavior at higher temperatures because of F^- vacancies in it [2]. The halogen-based perovskite crystal structure was firstly realized in CsPb X_3 in 1958 [7].

Oxides and fluorides-based perovskites are one of the most common crystal structures in the field of solid-state physics that can easily be synthesized. These can also be synthesized by the Bridgeman method or by the flux method to obtain single crystals [8]. $KCaF_3$ has a simple cubic structure where larger cation K is present at eight corners of the cube, smaller cation Ca is located at octahedral positions at the center of the

* Corresponding author.
E-mail address: rizwan.sps@pu.edu.pk (M. Rizwan).

https://doi.org/10.1016/j.mssp.2023.107363
Received 4 June 2022; Received in revised form 25 January 2023; Accepted 27 January 2023

cube, and fluorine is located at six face centers of the cube [9].

Lead-based organic-inorganic hybrid perovskites have emerged as promising materials for memory devices, and automobiles, especially in solar cells [10]. Instead of the many advantages of lead-based perovskites, these have some drawbacks such as device instability and the toxic nature of lead. The use of lead can be harmful therefore, in new research other materials are used and studied [11]. $KCaF_3$ being lead-free material has attracted new application domains and fields of science. To understand the nature of high conductivity in $KCaF_3$ crystal structure, numerous studies have been carried out in the literature. Using the single-crystal neutron diffraction technique not only the nature and concentration of defects in KCa F_3 were identified but also results explained mobile vacancies are responsible for high conductivity in these materials [12]. In 1994 G W. Watson et al. [13] used molecular dynamics simulations to investigate the effect of pressure on ionic conductivity of KCa F_3 with both defects consisting and defect-free models. In 1997 Raman spectra were studied between 40 and 700 K by PH. Daniel et al. [14] study high-temperature structural instabilities in KCa F_3 crystal structure. Halide perovskites like KCa F_3 have gained considerable attention as a phase transition in these crystals is different from other perovskites. By using an X-ray diffractometer and the Rietveld profile method; it was studied that tilting of Ca F_6 octahedra about a major crystallographic axis is responsible for distortion and phase transition in KCa F_3 cubic perovskite structure [15,16]. Firstly, in 2002, ab initio band calculations implemented in the VASP package were performed for various fluoroperovskites with LDA approximation and ultrasoft pseudopotentials. The observed bandgap for KCaF3 was indirect having a value of 6.21eV [17]. In 2011 electronic and optical properties of KCa F_3 were studied by Bahattin. Erdnic using DFT under ABNIT code. Lattice parameter (LP) with the value of 4.5293 **Å** was observed [9]. After one-year same physical properties were investigated for three materials MCa F_3 $(M = K, Rb, Cs)$ with DFT under wien2K code by applying GGA functional. Here decrement in the lattice parameter was observed having a value of 4.424**Å** by Wu-Cohen (WC-GGA) [18]. Electronic, elastic, and optical properties of KCa F_3 were also calculated by Soleimanpour et al. account by mBJ coupled with GGA approximation in Wien2K. The main purpose of this study was to compute elastic constants of KCa F_3 that were neither being computed before. Using the mBJ approach LP of 4.45 **Å** was observed which had a small difference from previously calculated results [6]. In the same year, structural, electronic, and elastic properties were computed for two materials KCa F_3, and RbCaF3 under Wien 2K by adding exchange-correlation effects through LDA, GGA-PBSol, and mBJ exchange potential. Results calculated through these exchange potentials were in agreement with available experimental data [19]. H. Bouafia et al. [3]studied the physical properties of KCa F_3, NaCa F_3, and $K_{0.5}Na_{0.5}$ CaF_3 whose results manifest an indirect bandgap for all materials having high values for LDA approximation than calculated through PBE-GGA. B. Ghebouli was the first to study structural, elastic, and optoelectronic properties of the family XCa F_3 $(X = K \text{ and } Rb)$ using DFT under CASTEP code representing LP of 4.3236**Å** calculated through GGA-PBE functional [4]. Ziu Li et al. calculated the properties of ten perovskite crystals using the CRYSTAL09 program. His calculations manifest that lattice parameter increase with the increase in ionic radii of studied materials while elastic constant and bandgap decrease. Calculated bandgap and lattice parameter for KCa F_3 were 4.4175 Å and 8.4377eV respectively [20]. In 2020, virtual crystal approximation and supercell doping methods were employed to see the variation in bandgap with doping amount. After supercell doping material bandgap not only decrease from 6.151eV to 4.9eV but also changed its nature from indirect to direct. Also, an increment in lattice constant was observed for the GGA-PBE approach than calculated through GGA- PBESol [5].

Reviewing the above literature and keeping the applications of pristine KCa F_3, it is a fact that this material is a wide bandgap material that limits its applications. Thus, impurity-induced $KCaF_3$ is studied by various researchers to minimize the bandgap of the $KCaF_3$ crystal structure [5]. Generally, impurity elements are doped either on A or B sites in perovskites depending on substitution criteria but another approach of replacing an anion with an impurity anion may help to reduce the bandgap and make the material more useful. The aim of this work is an inspiration to test the Br substitution at F sites gradually to reduce bandgap using density functional theory. The structural simplicity and symmetry of cubic phase $KCaF_3$ make it an ideal material for various application perspectives. Therefore, the main objective of this work was to perform bandgap engineering to explore its optoelectronic response to various optical materials. This is the first theoretical study of Br-substitution at the anionic site of c-$KCaF_3$ where a comprehensive comparison of electronic properties was made for both GGA and HSE03 formalisms to evaluate more reliable results. The novelty of this work was to study physical properties via halide substitution at anionic site gradually and then give a specific focus to observe the effect of these substitutions on these properties. After comparing our results with previous existing literature, it also has been noticed that this is a first-ever DFT study to predict photocatalytic properties using a band edge diagram to manifest a presented series of materials, useful candidates for hydrogen evolution reaction (HER), and oxygen evolution reaction (OER). Photocatalytic characteristics for different compositions ($x = 0, 0.6, 1.2, 1.8, 2.4, 3.0$) support E_g calculations, indicating that deduced doped materials could be used in solar cells and are essential for high photovoltaic efficiency. Br substitution at the anionic site of $KCaF_3$ is preferred over most of the other halides as it contains a lower band gap in the range of 3eV and is an ideal and beneficial crystal structure.

Bromine being a less electronegative element when substituted at the anionic site of $KCaF_3$ increases the nature of the covalent bond and all physical properties of perovskites are strongly affected by covalency [21]. By replacing F atoms with Br atoms, all physical properties especially optical properties can be tuned up. At 100% substitution, a new end material ($KCaBr_3$) is obtained whose bandgap is much less than pure material, as bandgap greatly depends upon chemical composition in a nonlinear manner. The effect of impurity under different doping ratios on properties of pure $KCaF_3$ is critical hence, results obtained in this study of KCa Br_3 would provide a valuable contribution to the literature and will motivate scientists for further research findings on this material.

The paper is organized in the following way: in section 2 explanations of computational detail and method is described, results and discussions of presented work are handled in section 3, and a summary of computed results is presented in section 4.

2. Computational details

Self-consistent calculations in the framework of density functional theory are performed in the CASTEP (Cambridge Sequential Total Energy Package) module of the material studio package based on the plane-wave pseudopotential method [22]. KCa F_3 is among the most symmetrical cubic structures belonging to the space group of Pm-3m. It contains five atoms in primitive cell having Wyckoff positions K (0,0,0), Ca (0.5, 0.5, 0.5) and F (0, 0.5, 0.5) [3,23]. The coordination number of Ca and K is six and twelve with F respectively while Fluorine has two with calcium [20]. To minimize the boundary effect in calculations a supercell of $2 \times 2 \times 1$ was constructed. A unit cell is shown in Fig. 1. Interaction of electrons with ions can be performed by using ultrasoft pseudopotential for K, Ca, and F atoms that can minimize the number of base planes in convergence calculations to retain computing methods. Exchange correlation potential effects were tackled within the generalized gradient approximation proposed by Perdew Burke and Ernzerhof (PBE) [5,24]. Plane-wave basis cutoff energy that explains the segregation of valence and core states [25] was set to 353.7 eV to optimize the c-KCa F_3 perovskite crystal structure [22]. Monkhorst-Pack scheme k-point mesh sampling was adjusted at $6 \times 6 \times 6$ to study the irreducible Brillouin zone. Self-consistency for geometry optimization is considered

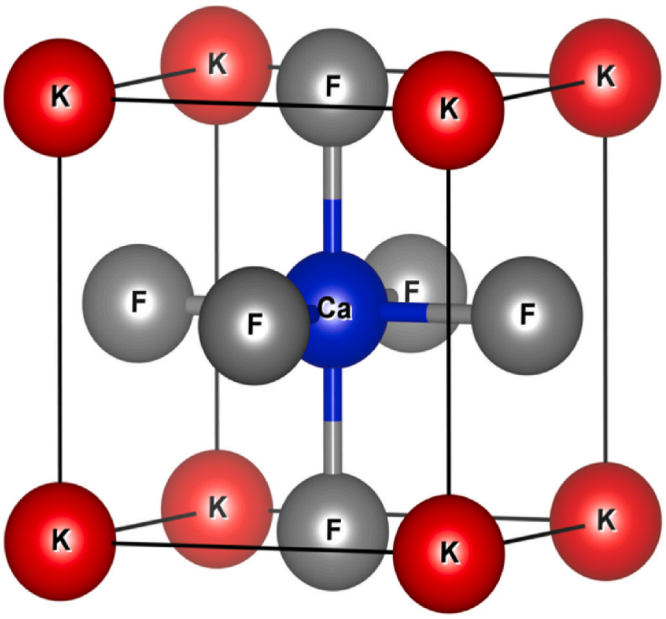

Fig. 1. Unit cell of pure KCa F_3, Red balls represent K, Blue at body center Ca, and face-centered grey balls represent fluorine. (For interpretation of the references to colour in this figure legend, the reader is referred to the Web version of this article.)

to be converged only when the total energy of the system is stable so convergence parameters were set in the following way: convergence tolerance of energy is within 2×10^{-5} eV per atom to avoid charge leakage, maximum applied stress and displacement are 0.1 GPa and 0.002 Å respectively and residual forces per atom were set to be 0.05 $eV/\mathring{A}$. Only valence electronic configuration is taken under observation as all physical properties are only affected by valence electrons so valence electronic configuration for all involved elements is given as follows: ($3s^2$, $3p^6$, $4s^1$) for K, ($3s^2$, $3p^6$, $4s^2$) for Ca and ($2s^2$, $2p^5$), ($4s^2$, $4p^5$) for F and Br respectively [1]. To study the effect of impurity inclusion on KCa F_3, Br atoms are substituted in the host supercell in a progressive manner such that each atom of F is replaced with a Br atom. Br atoms are induced progressively and at 100% substitution, new material is obtained. In the physical properties of each substitution, there is a change in the chemical composition of the material that directly affects the behavior of the material [26,27]. So, mixed halide perovskite KCa $F_{3-x}Br_x$ where x denotes substitution concentration has been investigated and reported as per best of the author's knowledge.

3. Results and discussion

3.1. Geometry optimization

The crystal structure of KCa F_3 is linked to the lattice structure of fluorite Ca F_2, a perfect fast ion conductor at high temperatures [28]. Using a pseudopotential method based on DFT under GGA-PBE, an important structural parameter; equilibrium lattice constant of cubical fluoride perovskite $KCaF_3$ was calculated by minimizing the total energy of crystal for different values of lattice constants via Birch-Murnaghan equations [3]. After fitting total energy as a function of volume as shown in Fig. 2 our calculated lattice constant for pure KCa F_3 is a = b = c = 4.31 Å. The computed lattice parameter is in reasonable agreement with the theoretical and experimental reports that are reported earlier, presented in table-1. Good agreement of presented results with reported theoretical data confirms the reliability of the method used herein. Optimized lattice parameter increases due to Br inclusion. At 100% substitution of Br, a new material with a higher lattice parameter is

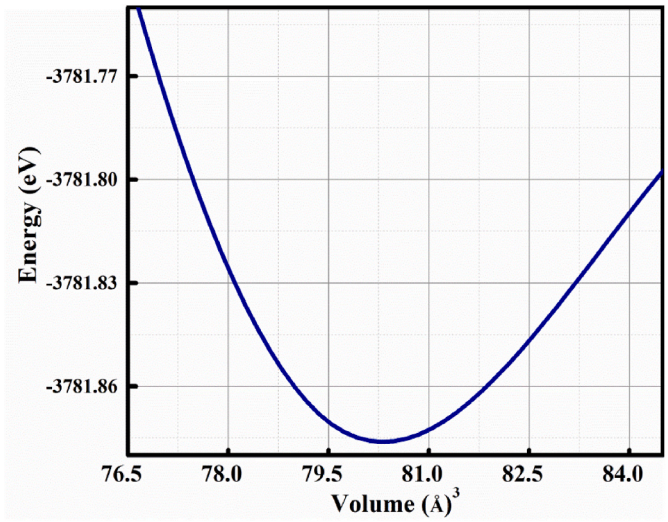

Fig. 2. Volume optimization curve for $KCaF_3$. (For interpretation of the references to colour in this figure legend, the reader is referred to the Web version of this article.)

obtained because the ionic radius of Br is greater than F. The difference in ionic radii of pure and Br substituted $KCaF_3$ gives rise to a difference in lattice parameters and according to doping criteria, this difference should be less than 30% [22]. A small difference in ionic radii causes a lesser effect on the lattice constant of supercell and maintains crystal symmetry respectively [29].

For the stable structure of the perovskite, the tolerance factor is calculated using an empirical index called the Goldschmidt relation [30]. The tolerance factor is given as:

$$t = \frac{(r_K + r_F)}{\sqrt{2}\,(r_{Ca} + r_F)} \quad (1)$$

Where r_K, r_{Ca}, and r_F, denotes ionic radii of K, Ca, and F atoms in the $KCaF_3$ crystal structure. Octahedral factor can also be used to discuss structural stability that is expressed: $H = r_B/r_X$. These two factors are a simple and useful approach to estimating the stability of perovskite structures. In the case of fluoro perovskites for high symmetry and to form perovskite structure t and H should have a range of 0.813–1.107 and 0.442 to 0.895 respectively [30,31]. Using Shannon's ionic radii [32] tolerance and octahedral factor for $KCaF_3$ are 0.901 [17] and 0.75 respectively these values show that our studied material has a stable cubic crystal structure.

A given perovskite crystal structure cannot exist in stable form until it follows relationships given by Born and Haung [6,33].

$$C_{11} - C_{12} > 0, C_{11} > 0, C_{44} > 0, C_{11} + 2C_{12} > 0 \quad (2)$$

Presented elastic constants calculated for cubic KCa F_3 perovskite crystal structure follows these stability criteria making it stable. For pure material, the values of C_{11}, C_{12}, and C_{44} respectively are 32.67155, -0.42155, and 88.8634 whereas at 100% substitution for new material, $KCaBr_3$; computed elastic constants are positive and fulfilled mechanical stability criteria as well. The values of C_{11}, C_{12}, and C_{44} respectively for $KCaBr_3$ are 223.35660, 29.56170, and 4.74015. Structure of doped material will considerably differ from pristine material due to many effects. Lattice parameter signifies spacing between adjacent unit cells that was observed more for doped material because of more ionic radii of Br. This increase in lattice parameter will change all optoelectronic properties. It will decrease bandgap as electrons will become less bound and less energy is required to make them free in conduction band. As a result, dielectric constant of new end material will also differ which depends on the electronic structure, density of atoms, and their

Table 1
Theoretical, Experimental, and present work (Theoretical) comparison of Geometric Components.

Material	Lattice Constant (Å) a = b = c	Volume $(Å)^3$	Functional	Reference
KCa F_3	4.31	80.063	GGA-PBE	Present work (Theoretical)
	4.31	80.063	LDA	Theoretical [2]
	4.32	80.621	GGA	Theoretical [4]
	4.32	80.621	LDA	Theoretical [19]
	4.32	80.621	LDA	Theoretical [34]
	4.38	84.024	–	Experimental [35]
KCa $F_{2.4}Br_{0.6}$	4.59	96.702	GGA-PBE	Present work (Theoretical)
KCa $F_{1.8}Br_{1.2}$	4.52	92.345	GGA-PBE	Present work (Theoretical)
KCa $F_{1.2}Br_{1.8}$	5.01	125.751	GGA-PBE	Present work (Theoretical)
KCa $F_{0.6}Br_{2.4}$	5.94	209.584	GGA-PBE	Present work (Theoretical)
KCa Br_3	5.73	188.132	GGA-PBE	Present work (Theoretical)

polarizability.

3.2. Electronic properties

Energy band structure and density of states are calculated to study the electronic nature of $KCaF_3$. Initially, GGA approach was applied to calculate band structures and corresponding density of states (DOS) of substituted element $KCaF_3$. However, utilizing GGA functional results obtained for electronic properties was dubious because of the substantial underestimation of bandgap in it. Studied materials may have a larger bandgap than the estimated one. To overcome intrinsic self-interaction errors, present in GGA functional, Heyd, Scuseria, and Ernzerhof hybrid functional (HSE) formalism was incorporated that rectifies errors by mixing some portion of Hartree-Fock exchange. Thus, standard calculations performed using the HSE approach provide more reliable results than other functionals [36]. Here standard HSE03 functional was incorporated. Band structures along high symmetry points in the first Brillouin zone utilizing GGA and HSE03 formalism at equilibrium volume with Fermi level at 0 eV are shown in Fig. 3 and Fig. 4 respectively. CBM lies at G-valley and VBM lies near Z-valley for KCa F_3 that provides indirect behavior for both approaches. As possessed in table 2, computed wide bandgap of pristine with GGA is 5.638 eV which limits its practical application and also limits its conductivity and intrinsic carrier concentration. For a pristine material value of the bandgap using the HSE03

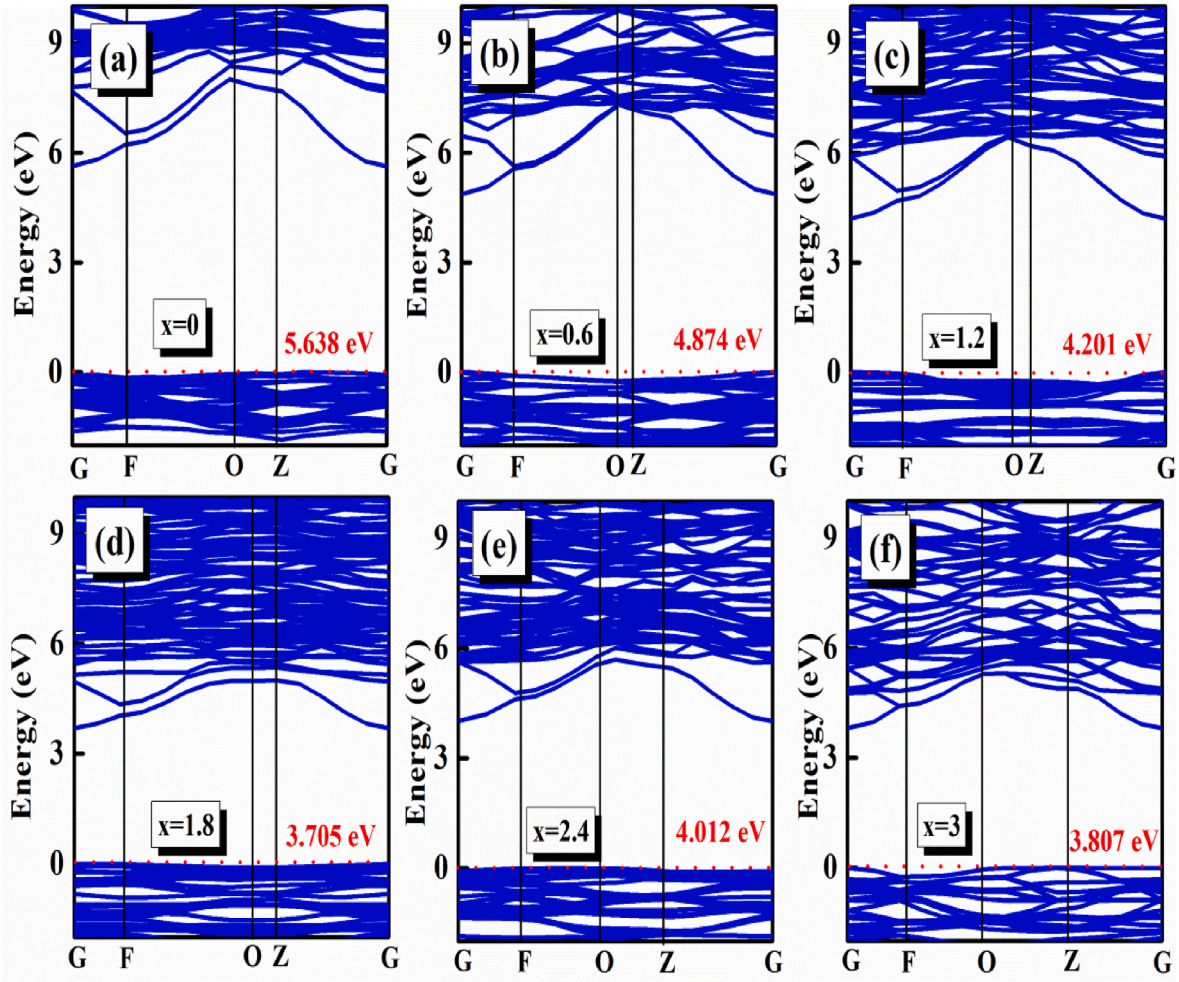

Fig. 3. Electronic band structures for KCa $F_{3-x}Br_x$ at different concentrations of x (x shows Br concentration) with GGA. (For interpretation of the references to colour in this figure legend, the reader is referred to the Web version of this article.)

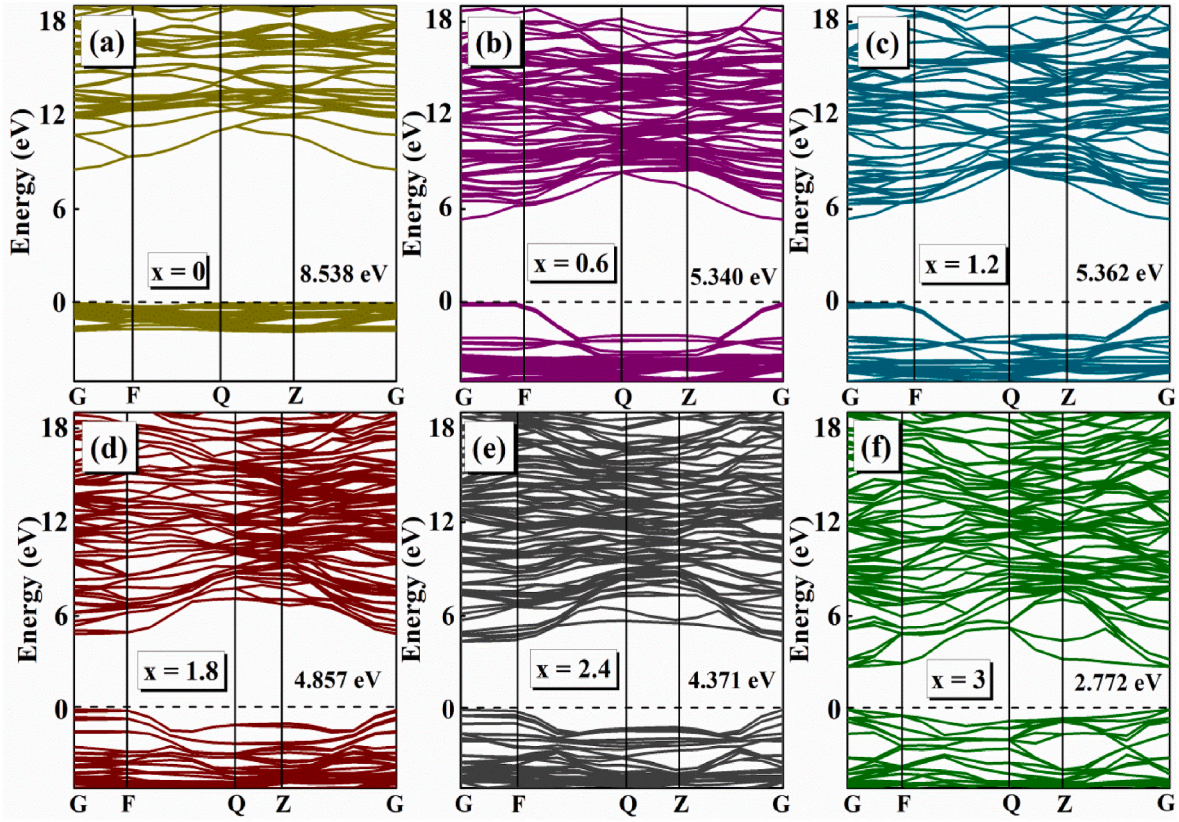

Fig. 4. Band structures along high symmetry points computed using the HSE03 approach. (For interpretation of the references to colour in this figure legend, the reader is referred to the Web version of this article.)

Table 2
List of bandgaps and optical parameters of substituted material $KCaF_{3-x}Br_x$ for all concerned concentrations compared with available literature.

Material	Bandgap (eV)		n (0)	ε' (0)	R (0) %
	GGA	HSE03			
KCa F_3	5.638	8.538	1.35	1.79	2
	5.94[a]	8.50[b]	1.39[c]	1.77[e]	1.6[b]
			1.39[d]	1.667[b]	
KCa $F_{2.4}Br_{0.6}$	4.874	5.340	1.44	2.10	3
KCa $F_{1.8}Br_{1.2}$	4.201	5.362	1.53	2.31	4
KCa $F_{1.2}Br_{1.8}$	3.705	4.857	1.53	2.38	4
KCa $F_{0.6}Br_{2.4}$	4.012	4.371	3	9.08	25
KCa Br_3	3.807	2.772	1.74	3.01	7

[a] Ref. [9].
[b] Ref. [18].
[c] Ref. [38].
[d] Ref. [1].
[e] Ref. [4].

approach is 8.538 eV which is much greater than calculated through the GGA approach. The presented bandgaps agreed well with previous experimental measured and theoretically calculated values [2,4,9,18]. Here hybrid functional (HSE03) is applied for the first time to calculate the electronic properties of KCa F_3 providing more reliable results close to experimental data. It is seen that the behavior of bandgap in $KCaF_3$ below Fermi level in the range -1.8-0eV is very appealing that is mainly occupied by F-2*p* states. Below valence band (VB), because of overlapping of electron wave functions, there is strong hybridization between F-2*s* and Ca-3*p* states that shows the performance of $KCaF_3$ which is greatly influenced by CaF_6 octahedron. $KCaF_3$ not only possesses a high ionic character but also shows a high degree of covalency in the Ca–F bond. All physical and chemical properties of the $KCaF_3$ structure are greatly influenced by this covalent behavior. The ionic model supposes that K cation loses an electron to fluorine anion to produce F^{-1} ions. So, the bandgap of $KCaF_3$ at equilibrium correlates to the electronic transition between K-4*s* and F-2*p* states. The lower part of the conduction band (CB) above the Fermi level is occupied by Ca-3*d* states with a small contribution of K-3p states. There is also a pure covalent bond between Ca-3d and K-3p states that leads to the partial occupation of d-orbitals that were empty in the ionic model. Bandgap of $KCaF_{3-x}Br_x$ decreases from 4.874 eV to 3.705 eV with increasing x (x = 0.6, 1.2, 1.08) for GGA approximation. With HSE03, bandgap is varied having values of 5.340, 5.362, 4.857, 4.371, and 2.772 eV respectively for all studied substitutions as elaborated in table 2.

By changing lattice parameters bandgap can be tuned. Due to the large ionic size of Br, after the replacement of Br atoms with F atoms band gap is decreased. As atomic size increases interatomic distance will also be increased which leads to less binding force between valence electrons and the parent atom. Since valence electrons are less bound; minimum energy is required to make them free inside the crystal which results in shrinkage of separation between a conduction band and valence band. For x = 0.6 and 1.2, a direct bandgap was observed with valence band maximum and conduction band minimum at G. New occupied cationic *d*-orbitals play a prime role in configuring the transition of bandgap from indirect to direct. As Br is substituted at the anionic site, a discrete acceptor level is created just below the valence band that starts to merge with other energy levels as substitution is increased and can be seen more clearly for HSE03 approximation.

At 100% substitution of Br at the F site ($KCaBr_3$), an indirect bandgap of 3.807 eV was observed for GGA having a valence band edge near Z in between Q and Z symmetry points and a conduction band edge at G. With HSE03 approach, an unexpected decrease in bandgap was observed for substituted concentration of 100% where bandgap decreases profoundly from 3.807 eV (calculated through GGA) to 2.772 eV

(calculated through hybrid functional). This decrease in bandgap makes KCa Br_3 a material useful for photochemical and photocatalytic applications [37]. This decrease in bandgap can be rationalized as shifting of energy levels more towards low energy region giving a prominent redshift to conserve mass action law. Coulomb repulsions and exchange interactions between carriers cause narrowing of bandgap as carrier concentration increases in KCa F_3. With Br-content, CB energy levels become more concentrated and disseminating because of hybridization between substituted electronic states and the conduction states. A large disseminating nature of electronic states is seen at conduction band minima while remarkably flat electronic states are noticed at valence band maxima that are an indication of high effective masses of valence band holes making low mobility of charge carriers as in crystals effective masses have an inverse relation with the curvature of the parabola. Value of bandgap estimates ionicity of perovskites. As bandgap decreases by increasing the concentration of Br in $KCaF_3$ crystal structure that shows $KCaF_3$ is more ionic than $KCaBr_3$ and covalent mixing in $KCaBr_3$ is more than $KCaF_3$ as covalent mixing decreased with an increasing bandgap.

To further clarify the origin of electronic band structure, total and partial density of states (TDOS, PDOS) have been computed using GGA and HSE03 formalism. Energy dispersal of different states can be understood with TDOS while participation of different states of atoms in different bands can be assessed using PDOS. Representation of TDOS and PDOS curves for pristine and non-pristine $KCaF_3$ including elemental PDOS is shown in Fig. 6. The conduction band was observed within energy range of 0–15 eV for the GGA approach. Both formalisms were providing the same results except that the Fermi level shifts more towards the valence band for the HSE03 formalism. Therefore, here GGA results will be described in detail. In GGA, conduction band was divided into two different parts; the lower one spans over the range 0–8eV, and the higher one spans over 8.1–15 eV. Conduction bands ranging from 0 to 8 eV, consist of K-4*s* and K-3*p* states while Ca-3*d* states are located at top of the conduction band (CB) that starts to shift towards low energy regions as substitution is increased. In DOS analysis it is found that Br induced material is p-type for all substitutions because of the presence of Fermi level close to the valence band edge. For different compositions (x = 0, 0.6, 1.2, 1.8, 2.4, 3.0) peak positions for conduction band are observed at 9 eV, 8 eV, 7.3 eV, 6.7 eV, 6.3 eV, and 13.0 eV respectively. The bandwidth of CB is not the same for all concentrations rather it is increasing because of the accumulation of new energy states. The valence band is observed in the energy range of (0 to -5 eV) which is our region of interest and can be configured as the top of VB. In the valence band region, the maximum peak in TDOS for pure $KCaF_3$ is observed at -0.35 eV which appears mainly due to the contribution of F-2*p* states. K-3*p* states along Ca-3*p* and F-2*s* states towards low energy region attributed to bottom of valence band and core states only owed to s-like states of K and Ca. These core states are occupied and usually do not play a significant role in determining the electronic properties of the material. In CB majority of contribution is from Ca-3*d* states having strong hybridization with K-3*p* states.

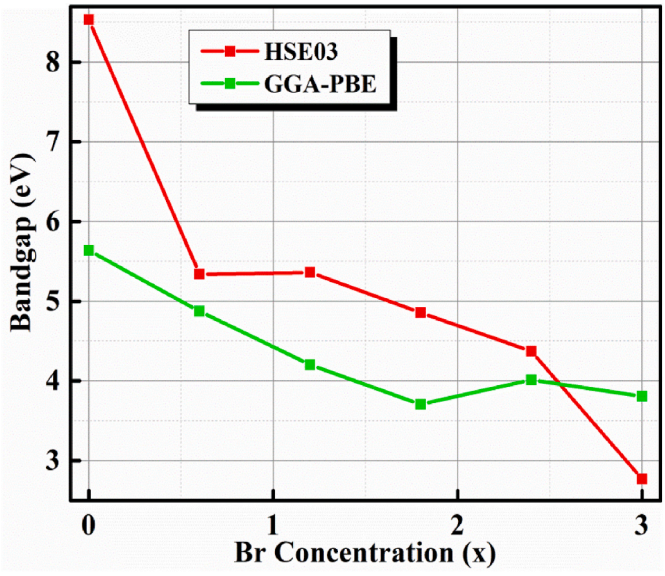

Fig. 5. Bandgap variation due to Br substitution. (For interpretation of the references to colour in this figure legend, the reader is referred to the Web version of this article.)

For x = 0.6, the bandgap is decreased because of less electronegativity of Br than F which changed the position of the valence band in such a way that the absorption edge moves towards a higher wavelength. Due to its high binding energy Br-4*s* states undergoes strong hybridization with Ca-3*d* states resulting in new energy states in the conduction band. In addition to the CB, bonding between K-3*p* states and Br-4*s* states also introduces new energy states in the VB. Peaks of BC are shifting towards lower energies showing a redshift in bandgap that results in a decrease in the bandgap.

As substitution concentration increase for GGA approach, band gap first decreases up to substitution of x = 1.8 then at x = 2.4 it starts to increase. Then for further substitutions, until all fluorine atoms are replaced with bromine atoms slight reduction in bandgap is observed. This nonlinearity in bandgap concerning substitution proportion is shown in Fig. 5. Utilizing HSE03, bandgap decreases linearly with each increase in Br-inclusion except for x = 1.2 which shows discrepancy here. This discrepancy can be attributed to a decrease in its lattice parameter from x = 0.6 concentration. This behavior of bandgap with Br-content that declined first up to a fraction of x = 1.8 with slightly rising for x = 1.2 then again decreasing fast for all other fractions of composition is also shown in Fig. 5.

From Fig. 6, it can be inferred that there is a negligible contribution in TDOS and PDOS by electrons of F in the region of the conduction band. CB was deduced from a mixture of all Ca-3*d*, Br-4*s*, K-3*p*, and K-4*s* states with different contributions. As substitution of bromine increases from x = 0.6 to x = 1.8, new states of bromine add in pure $KCaF_3$ causing a rise in all peaks. At 80% and 100% substitution contribution of bromine is dominant, showing the highest peaks comparable to that of x = 0. For x = 2.4, a slight increase in bandgap was observed because of the shifting of peaks in CB slightly towards higher energy indicating a blue shift in the bandgap. Absorption edge (Fermi energy level) is closer to the conduction band for further doping ratios absorption edge starts to deviate towards the valence band which can be explained via two important phenomena called Burstein moss shift and bandgap renormalization. At start, increase in bandgap and prominent blueshift can be attributed to Burstein moss shift due to occurrence of transition of electrons from valence band to occupy those states that are near to valence band and are vacant. More P-character and redshift was observed as substitution was increased because of shifting of fermi level toward valence band to conserve mass action law. This decrease in band gap or redshift is often attributed to bandgap renormalization. This effect happens because of more coulomb repulsions, more many-body effects or exchange interaction between carriers, as carrier concentration will increase in KCa F_3. For more inclusions hybridization between substituted electronic states and conduction states also play a critical role in increasing bandgap renormalization. Increase in hybridization between Br-4s and Br-4p states and pristine states was observed for higher concentrations that cause more covalent mixing in the material. F-2p states have only contribution in valence band whose intensity start to decrease with increasing concentration of Br states. Because of the negligible contribution of d-orbitals in VB, these are not shown in the figure.

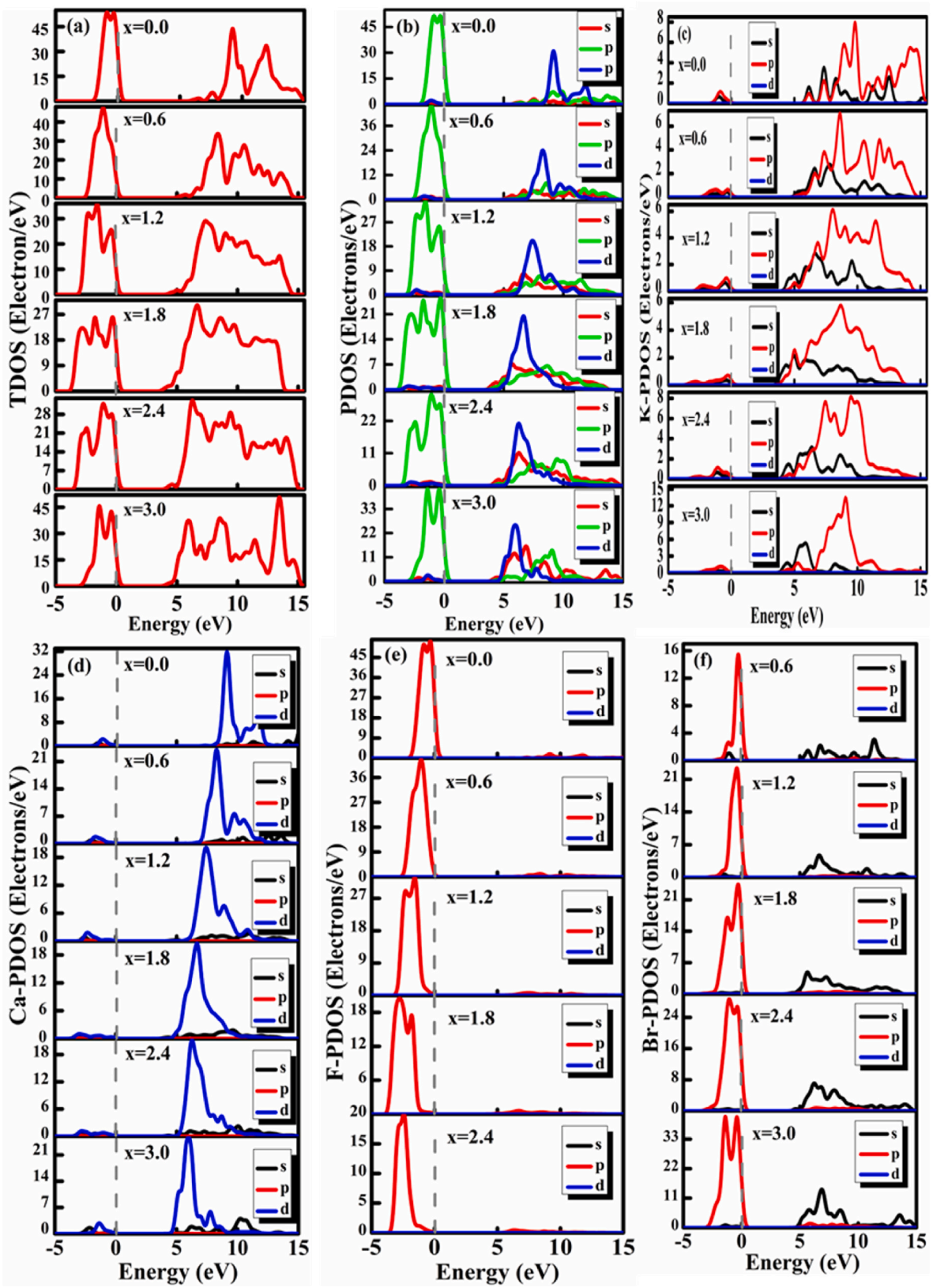

Fig. 6. Representation of (a–b) TDOS and PDOS of pristine and substituted $KCaF_3$ (c–f) elemental PDOS of K, Ca, F, and Br respectively at different concentrations of substitution in $KCaF_{3-x}Br_x$ (results obtained from GGA functional calculations). (For interpretation of the references to colour in this figure legend, the reader is referred to the Web version of this article.)

3.3. Optical properties

To get complete information about occupied and unoccupied regions of electronic band structure optical properties are studied. These properties originate directly as a result of wave matter interaction. Dielectric function (DF) is very useful to determine the complete band structure of a crystal. As compared to the shortest reciprocal lattice wave vectors of radiation in infrared, visible, and ultraviolet regions of the electromagnetic spectrum is very small therefore generally it can be taken as zero [39]. Important linear optical characteristics like absorption, reflection, loss function and refractive index can be computed knowing complex dielectric function [40]. To evaluate pure and Br substituted material optical response; real (ε') and imaginary (ε'') parts of DF at zero wave vectors as a function of electromagnetic wave frequency can be written as:

$$\varepsilon(\omega) = \varepsilon'(\omega) + i\varepsilon''(\omega) \tag{3}$$

ε'' can be calculated by adding all transitions from occupied to unoccupied states whereas ε' can be derived from the imaginary part of DF by using Kramer-Kronig transformations.

All observed characteristic peaks of optical parameters can be described by analyzing band structure and DOS of $KCaF_{3-x}Br_x$. At normal incidence refractive index $n(\omega)$ and extinction coefficient $K(\omega)$ is related to reflectivity coefficient $r(\omega)$ by:

$$R(\omega) = \frac{n + iK - 1}{n + iK + 1} \tag{4}$$

Refractive index and absorption coefficient are interlinked with each other these can be calculated from real and imaginary parts of a single parameter, called complex refractive index [41]. Following expressions are used to find out optical parameters like absorption coefficient I(ω), reflection coefficient R(ω), refractive index $n(\omega)$, extinction coefficient $K(\omega)$, and energy loss function L(ω) of material [42]:

$$I(\omega) = \sqrt{2}(\omega)\left[\sqrt{\left((\varepsilon'(\omega))^2 + (\varepsilon''(\omega))^2\right)} - \varepsilon'(\omega)\right]^{\frac{1}{2}} \tag{5}$$

$$n(\omega) = \left[\frac{\sqrt{\left((\varepsilon'(\omega))^2 + (\varepsilon''(\omega))^2\right)} + \varepsilon'(\omega)}{2}\right]^{\frac{1}{2}} \tag{6}$$

$$K(\omega) = \left[\frac{\sqrt{\left((\varepsilon'(\omega))^2 + (\varepsilon''(\omega))^2\right)} - \varepsilon'(\omega)}{2}\right]^{\frac{1}{2}} \tag{7}$$

$$L(\omega) = \frac{\varepsilon''(\omega)}{(\varepsilon'(\omega))^2 + (\varepsilon''(\omega))^2} \tag{8}$$

Optical properties of pure and Br-substituted $KCaF_3$ computed by ignoring phonon contributions and concerning only electronic transitions are shown in Fig. 7. All-optical constant spectra are analyzed and discussed in a photon energy range of 0–35 eV using a calculated band structure.

The absorption coefficient determines how far light of a particular wavelength can penetrate inside material before it is absorbed. The absorption process converts electromagnetic radiation into different forms depending upon the frequency of coming radiation and the material involved. Fundamental absorption involves an electronic transition between filled and unfilled energy states of material [43]. The threshold point in spectra occurs at 4eV, after Br inclusion, the material starts to absorb radiations sharply showing fluctuating spectra to reach maximum values. Absorption peaks of pure material are located at 9.98 eV, 12.1 eV, 19.9 eV, 22.4 eV, 26.2 eV, and 28.5 eV. With a Br substituting amount of 20% (x = 0.6), a new peak appears at 14.1 eV and the 22.4 eV peak shifts to 21.8 eV corresponding to redshift. Peak at

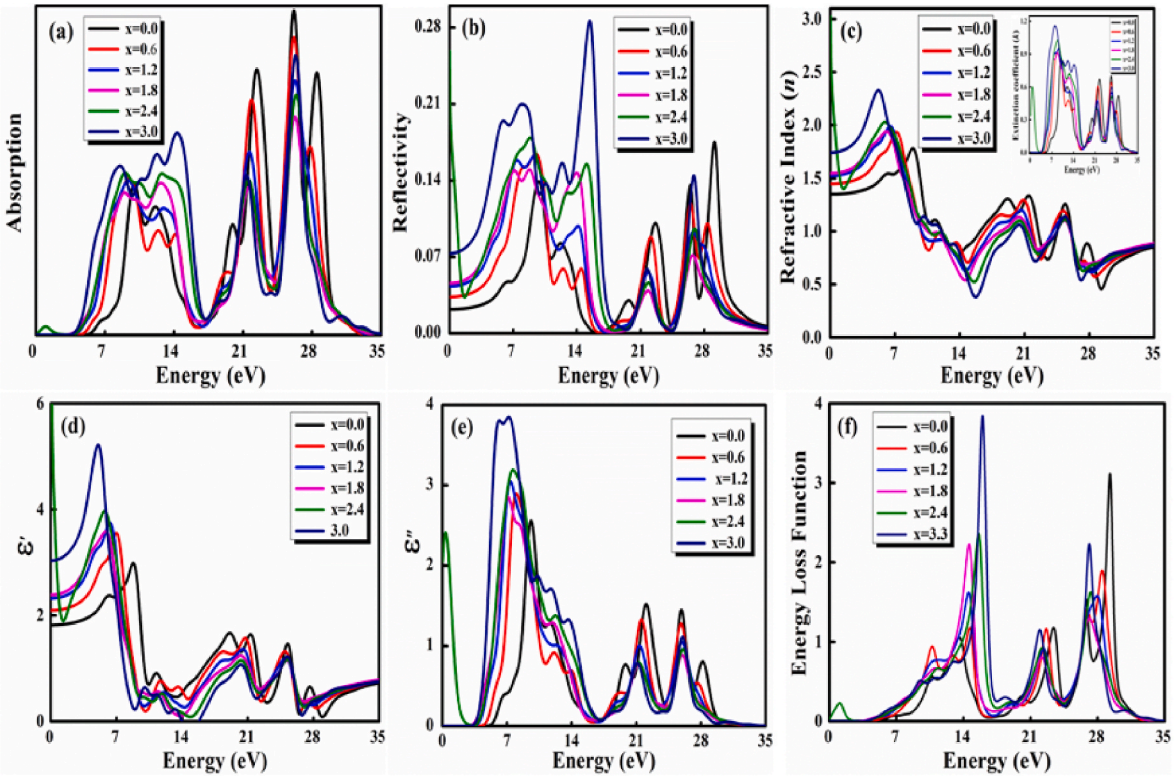

Fig. 7. Optical parameters are computed **(a)** Absorption co-efficient **(b)** Reflectivity **(c)** Refractive index along with extinction co-efficient **(d)** Real part of dielectric function **(e)** Imaginary part of dielectric function **(f)** Energy loss function. (For interpretation of the references to colour in this figure legend, the reader is referred to the Web version of this article.)

19.9 eV disappears and at 26.2 eV and 28.5 eV slightly shifted to 26.1 eV and 27.8 eV respectively. For x = 1.2, 1.8 and 2.4, peaks at 19.9 eV and 28.5 eV vanishes and the remaining peaks slightly shifted from observed pure peaks such as; for x = 1.2, peaks at 9.98 eV and 22.4 eV shifted towards lower energies at 9.37 eV and 21.5 eV indicating redshift and peak at 26.2 eV does not change. Similarly, for x = 1.8, the peak at 9.98 eV slightly shifted to 8.92 eV and hence a redshift, second to 12.67, third stay same, fourth to 21.5 eV and fifth to 26.2 eV; similarly at x = 2.4, peaks at 12.1 eV and 26.2 eV slightly shifted to 9.04 eV and 21.5 eV respectively whereas absorption edges at 12.1 eV and 26.2 eV shifted towards the higher value of energies showing blue shift that coincides with a calculated bandgap. At 100% substitution, a new peak is observed at 14.3 eV, a peak at 9.98 eV shifted maximally towards lower energy showing redshift and the remaining peaks slightly shifted having new positions at 12.2 eV, 21.3 eV, and 26.3 eV. All compositions show similar behavior within the photon energy range of 25–28eV in the low-frequency ultraviolet region. $KCaF_{3-x}Br_x$ shows high transparency within the energy range of 15-14 eV as no absorption peak is observed in this region. Inter-band transitions of electrons from occupied valence states to unoccupied conduction states are responsible for main peaks in absorption spectra. Peaks within the energy range of 0–7 eV are due to electron transitions from F-2*p* states of the valence band to K-4*s*, K-3*p*, and Br-4*s* states in the conduction band. For 7.1–14 eV peaks may be due to the transition from F-2*p* states of VB to Ca-3d states in CB. Sharp peaks at higher energies may be attributed to absorption from K-3*p* together with Ca-3*p* states to CB.

Computed reflectivity spectra of pure and Br-doped $KCaF_3$ are displayed in Fig. 6(b). Zero-frequency limit of spectra R(0) shows that reflectivity of $KCaF_{3-x}Br_x$ at different concentrations (x = 0, 0.6, 1.2, 1.8, 2.4 and 3.0) is 2%, 3%, 4%, 4%, 25%, and 7% respectively as given in table-2. Except for x = 2.4, all other values stay below 10% up to 3eV indicating high transparency in the infrared and visible regions of the energy spectrum. Beyond 3 eV reflectivity increases by increasing Br concentration and the highest peak is observed for $KCaBr_3$ material at 15 eV. Maximum reflectivity spectra are observed in low photon energy ranges up to 16 eV making presented materials useful for solar heating to be used in thermoelectric applications [44,45]. For the 16–20 eV photon energy range, high transparency is observed having negligible absorption and reflection in this region also reflectivity remarkably depends upon the refractive index. Because of the small absorption coefficient in the transparent region extinction coefficient and imaginary part of dielectric function are also negligible that is the reason; complex refractive index and DF are taken as real in this region [41].

Propagation of light from an optical medium is characterized by two parameters called refractive index (*n*) and extinction coefficient. The refractive index and extinction coefficient (*K*) are interlinked with each other through a single quantity called the complex refractive index. Refractive index as a function of the frequency of light beam talks about transmittance of material. Calculated refractive indices of $KCaF_{3-x}Br_x$ that have the same frequency-dependence as a real part of DF are shown in Fig. 7(c). From table-2 it is seen that static refractive indices $n(0)$ for various x values are 1.35, 1.44, 1.53, 1.53, 3, and 1.74 respectively where pristine result coincides well with available experimental and theoretical literature. It is noticed that except for x = 2.4, $n(0)$ increases by changing the composition from x = 0 to x = 3.0. Beyond the zero-frequency limit, the $n(\omega)$ increases with noticeable fluctuations to reach maximum values and the highest refractive index is observed for new material $KCaBr_3$ at 5 eV having a value of 2.34. The highest $n(\omega)$ of $KCaBr_3$ shows that it is a less transparent material than other Br concentrations, especially from pure $KCaF_3$. For the 12–17 eV photon energy range observed $n(\omega)$is less than unity for all compositions showing that alloying material will become transparent in this low-frequency ultraviolet region [40].

As above 30 eV energy range $n(\omega)$ becomes constant as dielectric function goes to zero in this energy range. Refractive index is inversely related to bandgap that holds for all concentrations except for x = 1.8. The extinction coefficient implies how actively a material absorbs light at a particular wavelength. $K(\omega)$ spectra have a similar profile as that of the imaginary part of the dielectric function [46]. From Fig. 7(c) it is clear that a large extinction coefficient is observed for x = 3.0 at a photon energy value of 7 eV. The maximum value of $K(\omega)$ indicates that the material is highly absorbing. The zero value of $K(\omega)$ at the energy range of 2–5 eV shows that light passes straightly through the material while in the rest of the spectra non-zero value of $K(\omega)$ corresponds to the exponential decay of radiation in the material.

The real part of DF, $\varepsilon'(\omega)$, is considered an intrinsic characteristic of any material which explains the dispersion properties of the material. $\varepsilon'(\omega)$ indicates polarization inside the material and polarization strength will be greatly affected by different Br concentrations because of its material-dependent nature [9,38]. Fig. 6(d) explains the $\varepsilon'(\omega)$ for $KCaF_{3-x}Br_x$. With the increase of Br concentration, static dielectric constant $\varepsilon'(0)$ that is the electronic part of $\varepsilon'(\omega)$ increases from 1.79 to 3.0l as possessed in table-2 except for x = 2.4 that shows the separate behavior of $\varepsilon'(\omega)$ having a maximum value of 9.08. After the static dielectric function, peaks of $\varepsilon'(\omega)$ increase and go to maximum values of 2.9, 3.6, 3.7, 3.6, 3.9, and 5.2 for all concentrations of x respectively then it starts to decrease and shift towards higher values of energy and becomes smooth after some fluctuations. The main effect of Br was observed within the photon energy range of 3–9 eV showing a maximum peak for $KCaBr_3$. Because of a maximum peak at 100% substitution; $KCaBr_3$ can be used as a polarizer but the negative value of this peak shows a metallic character in that energy range [47].

The imaginary part of DF, $\varepsilon''(\omega)$, is linked with the dissipation of energy such as absorption. It provides information that how a material will respond when disruption is created by electromagnetic radiations [27,48]. It coincides directly with extinction co-efficient and absorption co-efficient as one can see from Fig. 7(e). Main peaks of $\varepsilon''(\omega)$ are observed at 2.5 for x = 0, 2.9 for x = 0.6, 3.05 for x = 1.2, 2.8 for x = 1.8, 3.1 for x = 2.4 and 3.8 for x = 3.0 corresponding to transition from valence band to conduction band. For $\varepsilon''(\omega)$ the optical response starts at 3 eV providing a threshold value for transitions from valence band to conduction band after it sharply increases in spectral lines is observed that is due to an abrupt increase in transitions [49]. $\varepsilon''(\omega)$ Spectral lines have been increased with an increase in Br-content in $KCaF_{3-x}Br_x$.

Inter-band transitions at those spectral lines that mostly consist of Plasmon excitation; to define non-scattering and elastic scattering of electrons (zero loss of energy) an important optical parameter electron energy loss function (EEL) is used [49]. $L(\omega)$ depicts characteristic Plasmon oscillations and energy loss of electrons passing through the alloy. Fig. 7(f) explains the $L(\omega)$ spectra of $KCaF_{3-x}Br_x$ at different alloying concentrations. No energy loss occurs below 5 eV as photon energy is less than a bandgap of material in this region. The highest peak known as the Plasmon resonance peak occurs at 15 eV for x = 3.0, also increase in the magnitude of Plasmon excitations is observed in changing composition from x = 0 to x = 3.0. Plasmon peaks in spectra explain characteristic features associated with plasma frequency and came out at those energies where photons are absorbed by material [9,50–54]. So, the presented material provides promising optical properties that will motivate further experimental efforts on this material.

3.4. Photocatalytic property

In this study, cation substitution was employed to change the photocatalytic activity of semiconductors for the elimination of environmental pollutants. A lower E_g can be employed to increase CB lowering capacity while also increasing photocatalytic activity. Because of its non-toxicity, physical and chemical stability, and ease of use, $KCaF_{3-x}Br_x$ is the best photocatalyst [55].

Band-edge placements, band gaps, and charge carrier mobility are all factors that influence semiconductor photocatalytic activity. There is a need to develop generally applicable design approaches for any catalytic

process, including band-edge positions and band gaps, so that photocatalytic semiconductor candidates can be identified. This research establishes a theoretical basis for improving semiconductor photocatalytic activity in order to decompose pollutants in the environment [56]. The strategy is determined by photocatalytic mechanisms, as indicated in Fig. 8. Electrons transfer in a semiconductor photocatalyst when the optical radiation energy is equal to or greater than Eg. VB electrons are injected into the CB from the valence band. As in Eq. (9), h^+ in VB was left in VB and thee$^-$ in CB was introduced. Respectively, h^+ and e^- are with oxidative capacity and reducing power [57].

$$KCaF_3 + h \;\; KCaF_3\,(e^- + h^+) \tag{9}$$

CBM, VBM (EPc, EPv) and E_g electrode potentials can be approximated by equation (10).

$$EPc\ (V\ vs.\ NHE) = 1.23 - E_g(eV)\,/\,2 \tag{10}$$

Fig. 8 shows total water splitting redox potentials at band edge sites. This means that certain materials have the ability to both reduce and oxidize water. For different pH values, a varied quantity of photon energy is required to execute a total water splitting mechanism. Pure $KCaF_3$ has an overall water splitting potential due to its wide Eg range. For Br doped $KCaF_3$, overall water splitting can be shown (GGA and HSE03). The most suitable doping in total water splitting is $KCaF_{3-x}Br_x$ since it consumes the most energy. To achieve solar pollution degradation, e^- reduction capability must be capable of producing superoxide acid ($-HO_2$) and superoxide anion radicals ($-O_2^-$), as shown in equations (11) and (12). Photogenerated holes (h^+) must be capable of oxidizing OH^- to produce reactive hydroxyl radicals ($-$ OH) according to equation (13) [58].

$$O_2 + H^+ + e^- - HO_2 \tag{11}$$

$$O_2 + e^- - O_2^- \tag{12}$$

$$OH^- + h^+ - OH \tag{13}$$

Both –OH and $-O_2^-$ are highly oxidised free radicals. The oxidation of a range of organic and inorganic carbon compounds produces water, carbon dioxide, and other non-toxic tiny organic molecules. As a result, E_g of a semiconductor photocatalyst affects the absorbed spectrum of sunlight. The larger the spectral range responsiveness to sunlight and the more efficiently it can utilize visible light, the narrower the bandgap. CB and VB should be placed in such a way that they reach redox capacity. As a result, the absorbed spectrum of sunlight is affected by the E_g of a semiconductor photocatalyst. Larger spectral range reactivity to sunlight and ability to use visible light more efficiently, narrower E_g. The positions of CB and VB should be chosen to attain the necessary redox capacity.

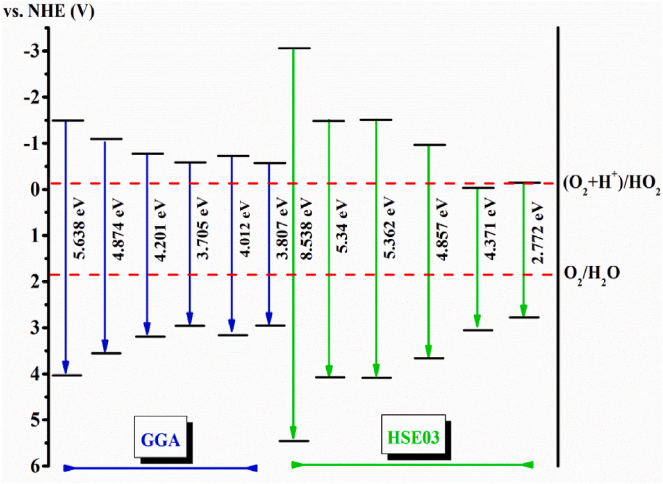

Fig. 8. Band edge potentials of pure $KCaF_{3-x}Br_x$ for hydrogen evolution reaction and oxygen evolution reaction potentials. (For interpretation of the references to colour in this figure legend, the reader is referred to the Web version of this article.)

The results support E_g calculations, indicating that pure and $KCaF_{3-x}Br_x$ materials have the best photocatalytic characteristics. We may also deduce that doped materials could be used in solar cells based on the findings.

4. Conclusion

First-principles calculations within GGA-PBE and HSE03 functional were implemented to compute structural and optoelectronic properties of $KCaF_{3-x}Br_x$ where x represents the concentration of Br. From the electronic band structure, it was inferred that except for 40% and 60% Br inclusion all other compositions possessed indirect bandgap having VBM and CBM at the different symmetry points of the irreducible Brillouin zone. With increasing concentration of Br, bandgap first decreases up to 3.705 eV then at x = 2.4, it starts to increase having a value of 4.012 eV showing that it changes nonlinearly with Br substitution amount. The bandgap of c-$KCaF_3$ can be tuned with different concentrations. A decrease in bandgap because of the shifting of peaks in the conduction band slightly toward lower energies by increasing the concentration of bromine shows that $KCaF_3$ is more ionic than $KCaBr_3$. Electronic properties of $KCaF_{3-x}Br_x$, are mostly influenced by F-2*p* states in the valence band and Ca-3*d* states in the conduction band. Tolerance factor, octahedral factor, and Born criteria lead to the stable cubic structure for both end materials *i.e.*, $KCaF_3$ and $KCaBr_3$. From the results of optical response, it is deduced that Br induced $KCaF_3$ has a trend toward high refractive index as well as reflectivity, which make the reported material a useful candidate for solar heating to be used in thermoelectric applications. A clear redshift was also observed in case of an increase in the concentration of Br. The study reveals that the presented material after inclusion of Br shows good photocatalytic response rather than pristine material. In conclusion, studying Br induced $KCaF_3$ allows researchers to acquire not only good optoelectronic properties but also a suitable bandgap value, which gives a theoretical foundation for future experimentation.

Author's agreement

All the authors are well agreeing with the content of the manuscript and there is no conflict of interest between authors.

Author's statement

It is stated that the work presented here is novel and is not under consideration for publication in any journal, in full or parts. We further testify that all the term and condition of the journal will be followed if it publishes in your esteemed journal.

CRediT authorship contribution statement

Seerat Fatima: Investigation. **Hafiz Muhammad Naeem Ullah:** Software, Investigation. **Abrar Ahmad Zafar:** Resources. **Zahid Usman:** Formal analysis, Data curation. **M.U. Farooq:** Writing – original draft, Validation. **Muhammad Rizwan:** Formal analysis, Conceptualization.

Declaration of competing interest

The authors declare that they have no known competing financial interests or personal relationships that could have appeared to influence the work reported in this paper.

Data availability

Data will be made available on request.

References

[1] A.A. Mousa, First-principles study of structural, electronic and optical properties of the $KCaX_3$ (X= F and Cl) compounds, Int. J. Mod. Phys. B 28 (2014), 1450139.
[2] A. Ali, A.U. Rahman, G. Rahman, Thermoelectric properties of $KCaF_3$, Phys. B Condens. Matter 565 (2019) 18.
[3] H. Bouafia, B. Sahli, S. Hiadsi, B. Abidri, D. Rached, A. Akriche, M.N. Mesli, Theoretical investigation of structural, elastic, electronic, and thermal properties of $KCaF_3$, $K_{0.5}Na_{0.5}CaF_3$ and $NaCaF_3$ perovskites, Superlattice. Microst. 82 (2015) 525.
[4] B. Ghebouli, M. Fatmi, M.A. Ghebouli, H. Choutri, L. Louail, T. Chihi, A. Bouhemadou, S. Bin-Omran, Theoretical study of the structural, elastic, electronic and optical properties of $XCaF_3$ (X= K and Rb), Solid State Sci. 43 (2015) 9.
[5] X. Liu, F. Jia, First principle study on electronic structure, elastic properties and debye temperature of pure and doped $KCaF_3$, Vacuum 179 (2020), 109504.
[6] S. Soleimanpour, F. Kanjouri, Elastic, electronic and optical properties of the cubic fluoro-perovskite $KCaF_3$ under pressure, Indian J. Phys. 89 (2015) 687.
[7] M. Ijaz, A. Shoukat, A. Ayub, H. Tabassum, H. Naseer, R. Tanveer, A. Islam, T. Iqbal, Perovskite solar cells: importance, challenges, and plasmonic enhancement, Int. J. Green Energy 17 (2020) 1022.
[8] S. Ogawa, The electron paramagnetic resonance of Mn2+ ions surrounded by an octahedron of fluorine ions, J. Phys. Soc. Jpn. 15 (1960) 1475.
[9] F.A. Modine, E. Sonder, W.P. Unruh, C.B. Finch, R.D. Westbrook, Phase transitions in $RbCaF_3$, Phys. Rev. B 10 (1974) 1623.
[10] B. Erdinc, Density functional calculations of the electronic band structure and optical properties of $KCaF_3$, GU. J. Sci. 24 (2011) 671.
[11] Busch-Vishniac, Trends in electromechanical transduction, Phys. Today 51 (1998) 28.
[12] T. Iqbal, S. Fatima, T. Bibi, M. Zafar, Graphene and other two-dimensional materials in advance solar cells, Opt. Quant. Electron. 53 (2021) 1.
[13] D.Z. Demetriou, C.R.A. Catlow, A.V. Chadwick, G.J. Mclntyre, I. Abrahams, The anion disorder in the perovskite fluoride $KCaF_3$, Solid State Ionics 176 (2005) 1571.
[14] G.W. Watson, A. Wall, S.C. Parker, A molecular dynamics simulation of the effect of high pressure on fast-ion conduction in a $MgSiO_3$-perovskite analogue; $KCaF_3$, Phys. Earth Planet. In. 89 (1995) 137.
[15] P. Daniel, M. Rousseau, J. Toulouse, Raman scattering study of potassium calcium fluoride $KCaF_3$, P*hysica Status Solidi (b)* 203 (1997) 327.
[16] H. Akiyama, M. Hidaka, Structural phase transitions in $KCaF_3$, Phase Transitions 27 (1990) 37.
[17] A. Ratuszna, R. Michel, D. Philippe, Crystal structure of $KCaF_3$ determined by the Rietveld profile method, Powder Diffr. 12 (1997) 70.
[18] G. Murtaza, A. Iftikhar, A. Afaq, Shift of indirect to direct bandgap in going from K to Cs in $MCaF_3$ (M= K, Rb, Cs), Solid State Sci. 16 (2013) 152.
[19] K. Yang, Y. He, Y. Cheng, L. Che, L. Yao, First-principles calculations on the structural and electronic properties of cubic $KCaF_3$ and $NaCaF_3$ (001) surfaces, Phys. Lett. 381 (2017) 890.
[20] K.E. Babu, N. Murali, K.V. Babu, B.K. Babu, M.V. Veeraiah, Structural, electronic and elastic properties of $KCaF_3$ and $RbCaF_3$ for vacuum-ultraviolet-transparent lens materials, AIP Conf. Proc. 1661 (2015), 100002.
[21] T. Wolfram, S. Ellialtioglu, Electronic and Optical Properties of d-band Perovskites, Cambridge University Press, 2006.
[22] X. Liu, J. Fu, M.M. Han, K.X. Sun, S.L. Wei, First-principles study on electronic structure, elasticity, debye temperature and anisotropy of cubic $KCaF_3$, Mater. Sci. Forum 999 (2020) 109.
[23] G. Arora, M. Sharma, Study of $KCaF_3$ and $CsCaF_3$ using hybrids density functionals, Mater. Today Proc. 29 (2020) 267.
[24] Z. Li, Y. Wang, D.X. Liu, First-principles study of the correlation between host Components and properties of $IAIIAF_3$ cubic perovskite compounds, J.Math. Inf. 9 (2017) 47.
[25] I. Zeba, R. Kiran, M. Shakil, M. Rafique, A. Riaz, S.S.A. Gillani, Study the effect of magnesium doping concentration on structural and optoelectronic response of $NaCa_{1-x}Mg_xF_3$ fluoro-perovskite: first-principles computation, Optik 218 (2020), 164990.
[26] K. Neupane, J. Himanshu, H. Lalhriatpuia, R.K. Thapa, Study of structural and electronic properties of $KCaF_3$ type fluoro-perovskite, Int. Res. J.Adv. Eng.Sci. 3 (2018) 345.
[27] M. Zafar, M.M. Kashif, M. Rizwan, Z. Anam, A. Shabbir, A. Arfan, C.B. Cao, M. Shakil, Theoretical study of structural, electronic, optical and elastic properties of $Al_xGa_{1-x}P$, Optik 182 (2019) 1176.
[28] M. Shakil, A. Arfan, I. Zeba, A. Riaz, S.S.A. Gillani, M.G. Asghar, Effect of mixed halide contents on structural, electronic, optical and elastic properties of $CsSnI_{3-x}Br_x$ for solar cell applications: first-principles study, Mater. Res. Express 7 (2020), 025513.
[29] R.E. Boyett, M.G. Ford, P.A. Cox, Molecular dynamics simulation of ionic conductivity in the fluoride-perovskite $KCaF_3$, Solid State Ionics 81 (1995) 61.
[30] N. Aeineh, E.M. Barea, A. Behjat, N. Sharifi, I. Mora-Seró, Inorganic surface engineering to enhance perovskite solar cell efficiency, ACS Appl. Mater. Interfaces 9 (2017), 13181.
[31] J.A. Abraham, DFT-focused estimation of mechanical, thermoelectric and thermodynamic properties of $ACdF_3$ (A= K, Rb, Cs) fluroperovskites, Int. J. Mod. Phys. B 33 (2019), 1950314.
[32] H. Tanaka, T. Oku, N. Ueoka, Structural stabilities of organic–inorganic perovskite crystals, Jpn. J. Appl. Phys. 57 (2018), 08RE12.
[33] D. Shannon Robert, Revised effective ionic radii and systematic studies of interatomic distances in halides and chalcogenides, Acta Crystallogr. A 32 (1976) 751.
[34] T. Nishimatsu, N. Terakubo, H. Mizuseki, Y. Kawazoe, D.A. Pawlak, K. Shimamura, T. Fukuda, Band structures of perovskite-like fluorides for vacuum-ultraviolet-transparent lens materials, Jpn. J. Appl. Phys. 41 (2002) L365.
[35] C.E.M. Campos, K. Ersching, J.C. De Lima, T.A. Grandi, H. Höhn, P.S. Pizani, Influence of minor oxidation of the precursor powders to form nanocrystalline CdTe by mechanical alloying, J. Alloys Compd. 466 (2008) 80.
[36] L. Li, D.X. Wang, C.G. Liu, M.G. Ma, A. Brik, M. Suchocki, Piasecki, A.H. Reshak, Comparative first-principles calculations of the electronic, optical, elastic and thermodynamic properties of $XCaF_3$ (X= K, Rb, Cs) cubic perovskites, Mater. Chem. Phys. 188 (2017) 39.
[37] P. Liu, C. Franchini, M. Marsman, G. Kresse, Assessing model-dielectric-dependent hybrid functionals on the antiferromagnetic transition-metal monoxides MnO, FeO, CoO, and NiO, J. Phys. Condens. Matter 32 (2019), 015502.
[38] A. Lamichhane, First-principles Density Functional Theory Studies on Perovskite Materials, PhD diss, New Jersey Institute of Technology, 2021.
[39] L. Yu, A. Zunger, Identification of potential photovoltaic absorbers based on first-principles spectroscopic screening of materials, Phys. Rev. Lett. **108** (2012), 068701.
[40] C. Kittel, Introduction to Solid State Physics, eighth ed., 2021.
[41] L. Azzouz, M. Halit, Z. Charifi, C.F. Matta, Tellurium doping and the structural, electronic, and optical properties of $NaYS_{2(1-x)}Te_{2x}$ alloys, ACS Omega 4 (2019), 11320.
[42] M. Fox, Optical properties of solids, Am. J. Phys. 70 (2002) 1269.
[43] D.M. Hoat, S. Rivas, A. Méndez B, First principles study of structural, electronic and optical properties of perovskites $CaZrO_3$ and $CaHfO_3$ in cubic phase, Solid State Commun. 275 (2018) 29.
[44] M.A. Wahab, Solid State Physics: Structure and Properties of Materials, Alpha Science Int'l Ltd., 2005.
[45] F. Hamioud, A.A. Mubarak, Structural, elastic and optoelectronic properties of the hydrogen based perovskite compounds: ab-initio study, Chin. J. Phys. 56 (2018) 1.
[46] A.A. Mubarak, First principles calculations of the electronic, optical and thermoelectric performance of $RbZn_{1-x}Ni_xF_3$ (x=0, 0.25, 0.5, 0.75 and 1) alloys, Int. J. Mod. Phys. B 33 (2019), 1950141.
[47] M. Zafar, M. Shakil, S. Ahmed, M.A. Choudhary, Ab initio study of structural, electronic and elastic properties of $CdSe_{1-x}S_x$ semiconductor, Sol. Energy 158 (2017) 63.
[48] N.S. Altshuler, S.A. Basoon, A.A. Karamyan, The dispersion of optical constants of the $KCdF_3$ and $KCaF_3$ crystals in the far infrared, P*hysica Status Solidi (b)* 70 (1975) K127.
[49] D. Sabba, H.K. Mulmudi, R.R. Prabhakar, T. Krishnamoorthy, T. Baikie, P.P. Boix, N. Mathews, Impact of anionic Br–substitution on open circuit voltage in lead free perovskite ($CsSnI_{3-x}Br_x$) solar cells, J. Phys. Chem. C 119 (2015) 1763.
[50] A. Toshniwal, V. Kheraj, Development of organic-inorganic tin halide perovskites: a review, Sol. Energy 149 (2017) 54.
[51] D.P. Rai, A. Shankar, P.S. Anup, T.P. Sinha, B. Merabet, R. Khenata, B. Arash, S. Shahram, R.K. Thapa, Electronic and optical properties of cubic $SrHfO_3$ at different pressures: a first principles study, Mater. Chem. Phys. 186 (2017) 620.
[52] A. Bouhemadou, O. Boudrifa, N. Guechi, R. Khenata, Y. Al-Douri, Ş. Uğur, B. Ghebouli, S. Bin-Omran, Structural, elastic, electronic, chemical bonding and optical properties of Cu-based oxides ACuO (A= Li, Na, K and Rb): an ab initio study, Comput. Mater. Sci. 81 (2014) 561.
[53] M. Naeem, M. Rizwan, R. Bakhtawar, U. Zahid, M. Xilan, C. Chuanbao, Oxynitride perovskite: computational approach to correlate structural, electronic, and optical properties of c-$BiAlO_3/N_3$, ACS.Appl. Electron.Mater. 4 (2022) 375.
[54] H.M.N. Ullah, M. Rizwan, S.S. Ali, Z. Usman, X. Ma, C. Cao, A computational study for mechanical, thermoelectric and optoelectronic applications of $BiAlO_3$ under static pressure, J. Phys. Chem. Solid. 168 (2022), 110819.
[55] J. Ge, Y. Zhang, Y.J. Heo, S.J. Park, Advanced design and synthesis of composite photocatalysts for the remediation of wastewater: a review, Catalysts 9 (2019) 122.
[56] S.G. Kumar, K.K. Rao, Comparison of modification strategies towards enhanced charge carrier separation and photocatalytic degradation activity of metal oxide semiconductors (TiO_2, WO_3 and ZnO), Appl. Surf. Sci. 391 (2017) 124.
[57] H. Yan, X. Wang, M. Yao, X. Yao, Band structure design of semiconductors for enhanced photocatalytic activity: the case of TiO_2, Prog. Nat. Sci.: Mater. Int. 23 (2013) 402.
[58] D. Venieri, A. Fraggedaki, M. Kostadima, E. Chatzisymeon, V. Binas, A. Zachopoulos, D. Mantzavinos, Solar light and metal-doped TiO_2 to eliminate water-transmitted bacterial pathogens: photocatalyst characterization and disinfection performance, Appl. Catal. B Environ. 154 (2014) 93.